High-resolution in vivo MR imaging of intraspinal cervical nerve rootlets at 3 and 7 Tesla

Julien Galley, Reto Sutter, Christoph Germann, Florian Wanivenhaus & Daniel Nanz

European Radiology

ISSN 0938-7994

Eur Radiol
DOI 10.1007/s00330-020-07557-3

Springer

European Radiology
https://doi.org/10.1007/s00330-020-07557-3

MUSCULOSKELETAL

High-resolution in vivo MR imaging of intraspinal cervical nerve rootlets at 3 and 7 Tesla

Julien Galley[1,2] · Reto Sutter[1] · Christoph Germann[1] · Florian Wanivenhaus[3] · Daniel Nanz[4,5]

Received: 16 July 2020 / Revised: 9 November 2020 / Accepted: 20 November 2020

Abstract

Objectives No routine imaging technology allows reliable visualization of nerve rootlets inside the spinal canal with positive contrast. The stronger MR signal at 7 T, with optimized protocols, may offer a solution. The purpose was to evaluate the potential of 3D Dual-Echo Steady-State (DESS) MR imaging of the cervical spine at 3 and 7 T in assessing the micro-anatomy of the nerve rootlets.

Materials/methods This prospective study was approved by the local ethics committee. Twenty-one patients, clinically referred to cervical-spine MRI, underwent additional MR exams at 3 T and 7 T, each of which consisted of a single 3D-DESS series with equal acquisition times. Artifacts, visualization quality, and number of identified rootlets (C2 to C8) were rated by two musculoskeletal radiologists. Results were compared by Wilcoxon tests. Interobserver reliability was assessed using weighted κ statistics and intraclass correlation coefficient (ICC).

Results Intraspinal rootlets could successfully be visualized at both field strengths. Rating differences for artifacts and quality of rootlet depiction were not significant for the two field strengths. The mean number of identified rootlets was larger for 7-T than for 3-T MR for every assessed nerve; however, this difference was not statistically significant using the Bonferroni correction (p values ranging from 0.002 to 0.53). Interobserver agreement was substantial to almost perfect (weighted κ values of 0.69 and 0.82). The ICC for the number of identified rootlets was 0.80.

Conclusion Non-invasive 3D-DESS MR-imaging at 3 and 7 T has the potential to provide precise assessments of the micro-anatomy of intraspinal cervical nerve roots.

Key Points

- *Cervical rootlets can be successfully visualized with positive contrast using 3D-DESS MR-imaging.*
- *3D-DESS MR-imaging at 3 and 7 T provides precise assessments of the micro-anatomy of cervical nerves.*
- *The mean number of identified cervical rootlets using 3D-DESS was larger for 7 T than for 3 T MR; however, this difference was not statistically significant.*

Keywords Magnetic resonance imaging · Spine · Nerve

Abbreviations

CSF	Cerebrospinal fluid
DESS	Dual echo steady state
ICC	Intraclass correlation coefficient
MIP	Maximum intensity projection
MPR	Multiplanar reformat
SAR	Specific absorption rate
STIR	Short tau inversion recovery
TE	Echo time
TR	Repetition time

✉ Julien Galley
galleyjulien@gmail.com

[1] Department of Radiology, Balgrist University Hospital, University of Zurich, Zurich, Switzerland

[2] Department of Radiology, HFR, University of Fribourg, Fribourg, Switzerland

[3] Department of Orthopedic Surgery, Balgrist University Hospital, University of Zurich, Zurich, Switzerland

[4] Swiss Center for Musculoskeletal Imaging (SCMI), Balgrist Campus AG, Zurich, Switzerland

[5] University of Zurich, Zurich, Switzerland

Published online: 06 January 2021

Introduction

Cervical spinal nerves are classified into 8 pairs (right/left) of nerves, called C1 to C8, as they emerge through the intervertebral foramen above the corresponding vertebral bodies, except for C8, which arises above the first thoracic vertebral body. Each nerve consists of the fusion of a ventral and dorsal root, each of which, in turn, is made of several distinct rootlets (or fila radicularia) that emerge from the spinal cord. Along the longitudinal axis of the cord, the rootlets arise anteriorly and posteriorly at quite regular intervals, with no apparent segmental organization, and laterally combine at each level in a "ponytail" manner to form the intra-spinal root [1]. The anterior rootlets are thinner than the posterior ones. The number of rootlets per posterior root was reported to vary from 2 to 13 with an average of 8 [2, 3]. The dorsal root enlarges into the dorsal root ganglion, which contains afferent nerve-cell bodies that relay sensory information from the peripheral nervous system to the central one. The most common pathology of the cervical nerve, radiculopathy or "pinched nerve," is caused by compression of a nerve root leading to pain, sensory/motor affection, or reflex changes. Common causes are cervical spondylosis and intervertebral disc herniation [4, 5]. In assessing radiculopathy, there is little doubt that magnetic resonance imaging (MRI) is the modality of choice [6]. In patients with major trauma of the cervical spine, nerve-root avulsions are the most concerning issues [7, 8]. Even if MRI is clearly indicated in cases of plexus injuries [9, 10], it is still limited and has only moderate accuracy in assessing traumatic nerve root avulsion [11]. Whereas MR imaging–based assessments of the extra-spinal nerves and the plexus by means of short-tau inversion-recovery (STIR)-based spin-echo imaging or by diffusion-weighted imaging [12–14] are well documented, there is currently no dedicated MR sequence to precisely image the intraspinal nerve-root components. They may occasionally be seen on T2-weighted spin-echo based images or on fully balanced gradient-echo images as fine dark bands that contrast against a bright cerebrospinal fluid. However, these are typically non-systematic incidental findings. A more consistent visualization of intraspinal nerve-root components in clinical routine could allow identification of normal healthy and pathological anatomical patterns and be useful for pre-surgical planning. The larger signal available for MR imaging at a high magnetic field of 7 T was already shown to enable high-resolution visualization of neurological structures [15–17] and to have a great potential in assessing cervical nerves. The purpose of the current study was to evaluate the feasibility of a positive-contrast visualization of the intraspinal cervical-nerve microanatomy with a dedicated MR scan at 3 T and 7 T, in a cohort of patients referred for clinical cervical spine MRI.

Materials and methods

This prospective study was approved by the local ethical committee. Written informed consent was obtained from all participants prior to the exams.

Study population

Patients presenting neck pain referred to our university hospital for clinical cervical spine MRI between September and November 2019 were asked to participate in the study. All participants were older than 18 years. Exclusion criteria were recent trauma, presence of fracture, or previous surgery of the cervical spine.

MRI

All patients underwent two consecutive short MR exams on the following MR units: a 7-T MR system (MAGNETOM Terra, Siemens Healthineers) with an 8-channel C-spine surface array transmit-receive coil (Rapid Biomedical GmbH) and a 3-T MR system (MAGNETOM Prisma, Siemens Healthineers with a 20-channel head/neck receive coil (Siemens Healthineers). Availability of the scanners determined the order of the scans at the 2 field strengths. A 3D dual echo steady state (DESS) sequence was acquired on both MR units. The imaging parameters are listed in Table 1. At both field strengths, the acquisition parameters were optimized by scans with phantoms and 3 asymptomatic volunteers. Standard CE-mark product sequences, not modified by the study team at the source-code level, were used. They suffered from different limitations at the two field strengths; hence, it was not possible to select two sets of fully "identical" parameters. E.g., exclusive water-signal excitation was only possible in combination with a spatially non-selective excitation pulse at 7 T, which required the coverage of a relatively large field of view to minimize signal aliasing. Also, the maximum flip angle was limited by specific absorption rate (SAR) constraints at a TR-dependent smaller nominal value at 7 T compared to 3 T. The quality of the intraspinal nerve-root visualization was found to significantly depend on the echo time and the excitation flip angle. Thus, striving for an as meaningful and interesting comparison as possible, the parameters were optimized as follows: at both systems, it was attempted to reach the system-specific maximum isotropic spatial resolution that still promised sufficient SNR within clinically acceptable scan durations in the testing phase. At the same time, it was attempted to keep the following parameters identical or as similar as possible: the acquisition time, the echo (TE) and repetition (TR) times, the covered imaging volume or field of view, and the read-out bandwidth (in units of "kHz", as opposed to in units of "Hz per pixel"). At 7 T, the maximum excitation flip angle possible given the SAR limitations was chosen.

Table 1 Imaging parameters of the 3D dual echo steady state (DESS) sequences acquired at 3 T and 7 T

Parameters	3T	7T
TR/TE (ms)	3.0 / 10.8	3.0 / 11.1
Excitation flip angle (degrees)	25	20
Imaged field of view (mm) (readout/phase/slab direction)	205 /185 / 115	200 / 181 / 101
Encoded voxel dimensions (mm)	0.80 × 0.80 × 0.80	0.63 × 0.63 × 0.63
Readout bandwidth (Hz/pixel (kHz))	296 (75.8)	237 (75.8)
Acquisition time (min:s)	06:29	06:38
Parallel-imaging acceleration factor	2	3
Acquisition orientation	coronal	coronal

TE echo time, *TR* repetition time

MR image analysis

MR exams were independently evaluated by two fellowship-trained musculoskeletal radiologists (6 and 7 years of experience in musculoskeletal imaging). Both readers were blinded to patient data, clinical information, and MR data. The MR exams were anonymized and presented in a randomized fashion on our institution's picture archiving and communication system (PACS). Each reader was first asked to evaluate the presence of artifacts using a 4-grade scale: *no* artifacts; *mild* artifacts: image quality still acceptable with detail detection possible; *considerable* artifacts: image quality limited, detail detection hampered; *severe* artifacts: image not analyzable.

The nerve rootlets were qualitatively and quantitatively assessed. A qualitative rating was first done by describing their general visibility: *sharp* (rootlets perfectly delineated and separable from each other, with good contrast with CSF) *moderate* (rootlets clearly identified with good contrast but some blurring), or *poor delineation* (rootlets not clearly definable). Then, a quantitative assessment was made by counting the number of visible rootlets per nerve root (from C2 to C8) at each of the 4 emergences (anteriorly/posteriorly, right/left) at each level. A rootlet was only taken into account if it could be visualized in continuity from the cord to the fusion of the anterior and posterior roots. The evaluation could be done in any plane using multiplanar reconstruction (MPR).

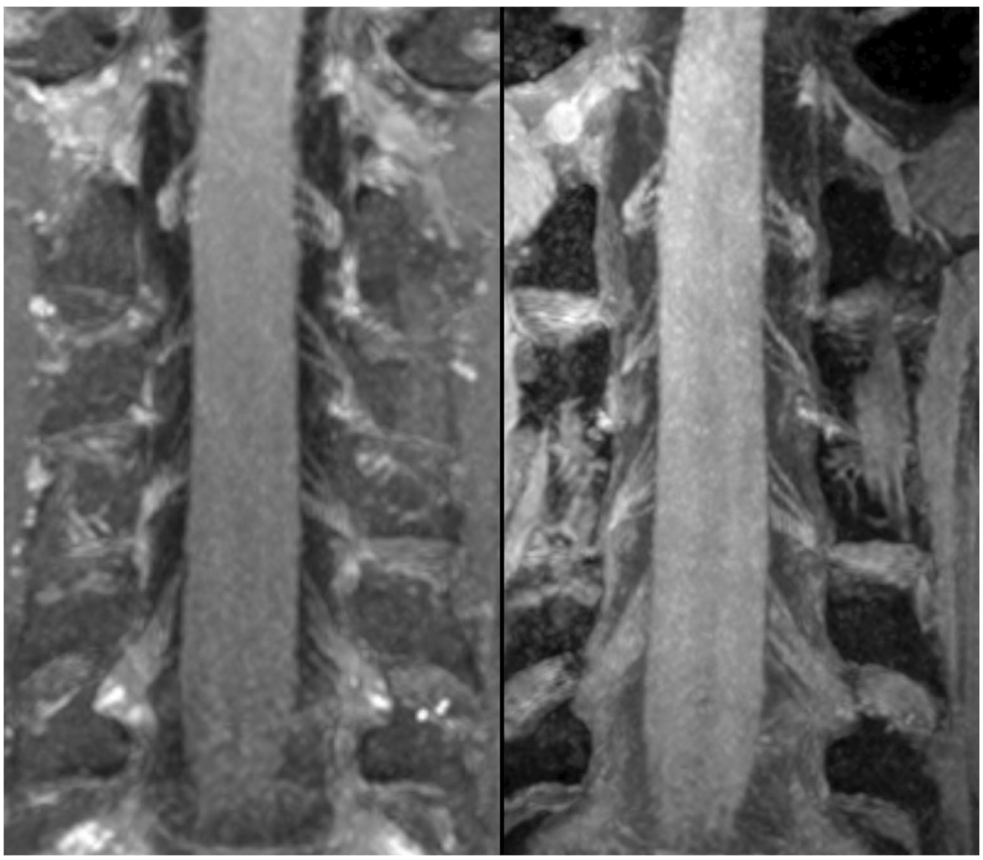

Fig. 1 Coronal 5.2-mm maximal intensity projection (MIP) images of a 34-year-old male patient with a visualization of posterior intraspinal nerve rootlets. *Left*: 3-T MRI. *Right*: 7-T MRI

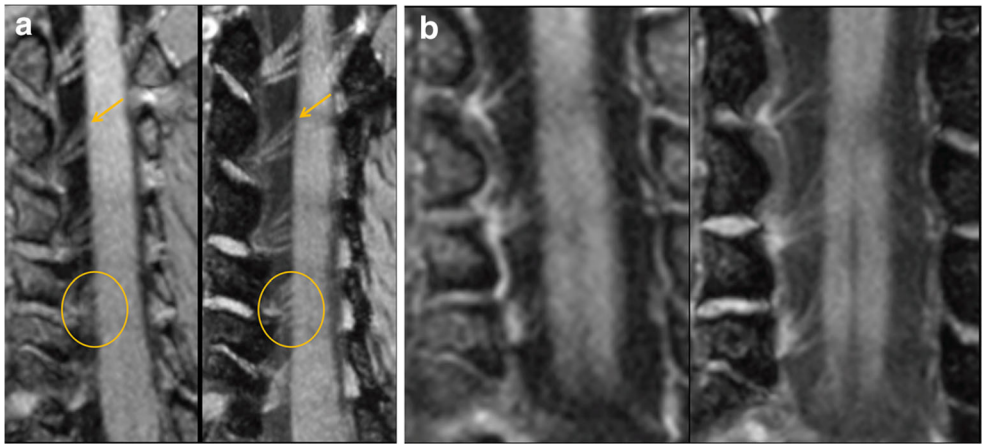

Fig. 2 **a** Coronal oblique 1.7-mm MIP reconstructed images of right *posterior* intraspinal nerve rootlets (C3 to C7) of a 48-year-old female patient. The 7-T image (*right*) allows a better distinction of the two cranial C4 rootlets (orange arrow) than the 3-T image (*left*) and provides a more detailed visualization of the C6 rootlets (orange circle)**. b** Coronal oblique reconstruction images (MPR without MIP) that show *anterior* right intraspinal nerve rootlets (C4 to C6) of a 48-year-old female patient (the same as in **a**). The 7-T image (*right*) offers a more detailed visualization of the rootlets than the 3-T image (*left*)

Statistical analysis

Statistical analysis was performed using SPSS (v23, IBM Corp.). Wilcoxon tests were used to compare the groups (3T vs 7T) regarding artifacts, subjective general visibility of rootlets, and the number of rootlets. As 28 rootlets were evaluated, p values were adjusted using the Bonferroni correction: a p value < 0.0017 (0.05/28) indicates a statistically significant difference.

The interobserver agreement was evaluated using weighted κ statistics for the artifact and rootlets delineation evaluation. For the number of rootlets, agreement was assessed using the intraclass correlation coefficient (ICC).

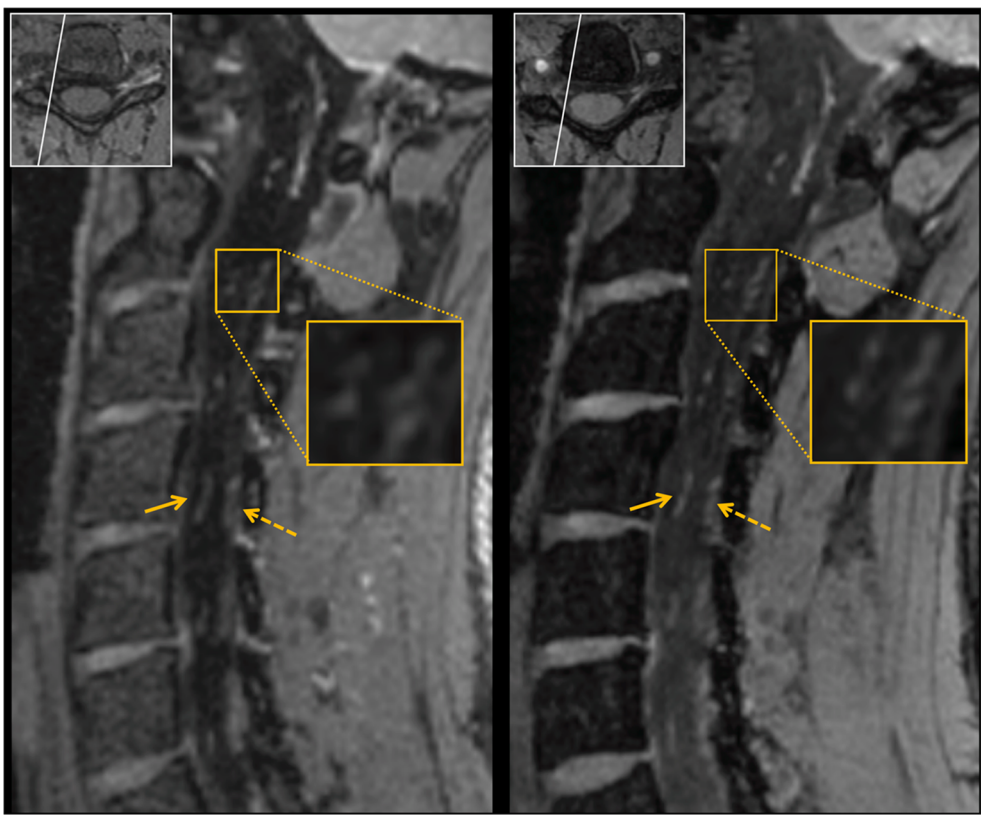

Fig. 3 Paramedian sagittal oblique images of a 30-year-old female patient. Both anterior (orange arrows) and posterior (dotted arrows) intraspinal nerve rootlets are visualized on 3-T (*left*) and 7-T (*right*) images. As shown in the enlarged area, the 7-T image offers a higher spatial resolution and allows for a better distinction of the rootlets

Results

Patient characteristics

One patient could not undergo the 7 T exam because of claustrophobia and was excluded from the study. Twenty-one patients, 9 women and 12 men, with a mean age of 49.2 ± 15.8 completed the study. Nine patients were first examined at 3 T and ten patients first at 7 T. The mean body mass index (BMI) was 25.5 kg/m^2 (range 19.3–33.0).

MRI findings

Artifacts

No difference was found between 3 T and 7 T exams regarding the artifact level for both readers (p values of 0.8 and 0.6). For most of the exams, the artifact level was rated either *no* ($N_{reader1,3T}$ = 10, $N_{reader1,7T}$ = 12; $N_{reader2,3T}$ = 11, $N_{reader2,7T}$ = 11) or *mild* ($N_{reader1,3T}$ = 9, $N_{reader1,7T}$ = 7; $N_{reader2,3T}$ = 7, $N_{reader2,7T}$ = 8). Few were classified *considerable* ($N_{reader1,3T}$ = 2, $N_{reader1,7T}$ = 2; $N_{reader2,3T}$ =

Table 2 Number of rootlets per root ± standard deviation for both readers. Ranges are in parentheses

Level	Emergence location		Reader 1			Reader 2		
			Number of rootlets		p value	Number of rootlets		p value
			3T	7T		3T	7T	
C2	Right	Ant	2.2 ± 0.5 (2–4)	2.4 ± 0.8 (2–5)	0.157	2.1 ± 0.7 (1–4)	2.4 ± 0.9 (1–5)	0.166
		Post	2.5 ± 0.5 (2–3)	3.1 ± 0.7 (2–5)	0.002*	2.3 ± 0.5 (2–3)	3.1 ± 0.7 (2–5)	0.000**
	Left	Ant	2.1 ± 0.8 (1–4)	2.3 ± 0.7 (1–4)	0.564	2.1 ± 0.6 (1–4)	2.3 ± 0.9 (1–5)	0.166
		Post	3.0 ± 0.9 (2–5)	3.2 ± 0.8 (2–5)	0.058	2.7 ± 0.7 (2–4)	3.1 ± 0.7 (2–5)	0.029*
C3	Right	Ant	1.6 ± 0.7 (1–3)	1.8 ± 0.5 (1–3)	0.366	1.5 ± 0.5 (1–2)	1.8 ± 0.5 (1–3)	0.083
		Post	3.0 ± 0.7 (2–4)	3.7 ± 0.8 (2–5)	0.002*	3.0 ± 0.7 (2–4)	3.7 ± 0.8 (2–5)	0.002*
	Left	Ant	1.6 ± 0.6 (1–3)	1.8 ± 0.5 (1–3)	0.206	1.7 ± 0.6 (1–3)	1.5 ± 0.5 (1–2)	0.366
		post	3.0 ± 0.3 (2–4)	3.6 ± 0.7 (2–5)	0.007*	2.9 ± 0.4 (2–3)	3.6 ± 0.9 (2–6)	0.007*
C4	Right	Ant	1.8 ± 0.6 (1–3)	1.9 ± 0.5 (1–3)	0.527	1.6 ± 0.6 (1–3)	1.9 ± 0.5 (1–3)	0.010*
		Post	2.4 ± 0.8 (2–4)	2.9 ± 0.6 (2–4)	0.029*	2.4 ± 0.7 (1–4)	3.0 ± 0.6 (2–4)	0.003*
	Left	Ant	2.0 ± 0.5 (1–3)	2.1 ± 0.5 (1–3)	0.414	2.0 ± 0.6 (1–3)	2.0 ± 0.6 (1–3)	0.480
		Post	2.5 ± 0.7 (1–4)	2.9 ± 0.5 (2–4)	0.033*	2.6 ± 0.5 (2–3)	3.1 ± 0.5 (2–4)	0.008*
C5	Right	Ant	2.3 ± 0.6 (1–3)	2.7 ± 0.7 (1–4)	0.123	2.1 ± 0.5 (1–3)	2.4 ± 0.7 (1–3)	0.058
		Post	2.8 ± 0.8 (1–4)	3.4 ± 1.0 (2–6)	0.003*	2.7 ± 0.8 (1–4)	3.5 ± 1.0 (2–6)	0.002*
	Left	Ant	2.2 ± 0.5 (1–3)	2.6 ± 0.8 (1–4)	0.052	2.1 ± 0.5 (1–3)	2.5 ± 0.8 (1–4)	0.071
		Post	2.6 ± 0.7 (1–4)	3.3 ± 0.8 (1–4)	0.002*	2.7 ± 0.7 (1–4)	3.2 ± 0.8 (1–5)	0.017*
C6	Right	Ant	2.0 ± 0.7 (1–3)	2.6 ± 0.7 (2–4)	0.008*	1.9 ± 0.6 (1–3)	2.5 ± 0.8 (1–4)	0.007*
		Post	2.9 ± 0.7 (2–4)	3.4 ± 1.0 (2–5)	0.012*	2.9 ± 0.9 (1–5)	3.4 ± 1.0 (1–5)	0.003*
	Left	Ant	2.0 ± 0.6 (1–3)	2.6 ± 0.9 (1–4)	0.003*	2.1 ± 0.7 (1–3)	2.4 ± 0.7 (1–4)	0.065
		Post	3.0 ± 0.7 (2–5)	3.4 ± 0.9 (2–5)	0.071	2.9 ± 0.9 (1–5)	3.3 ± 1.0 (1–5)	0.067
C7	Right	Ant	1.8 ± 0.7 (1–3)	2.2 ± 0.8 (1–4)	0.080	1.6 ± 0.6 (1–3)	2.0 ± 0.8 (1–4)	0.013*
		Post	2.5 ± 0.8 (1–4)	3.0 ± 1.0 (1–5)	0.053	2.5 ± 1.0 (1–6)	3.2 ± 1.0 (1–5)	0.036*
	Left	Ant	1.7 ± 0.7 (1–3)	2.1 ± 0.5 (1–3)	0.013*	1.7 ± 0.7 (1–3)	2.1 ± 0.8 (1–4)	0.029*
		Post	2.5 ± 1.0 (1–4)	2.9 ± 0.9 (1–4)	0.129	2.6 ± 0.9 (1–5)	3.1 ± 1.0 (1–5)	0.029*
C8	Right	Ant	1.3 ± 0.5 (1–2)	1.8 ± 0.5 (1–3)	0.002*	1.2 ± 0.4 (1–2)	1.7 ± 0.5 (1–2)	0.007*
		Post	2.1 ± 0.9 (1–4)	2.4 ± 0.9 (1–4)	0.027	2.3 ± 1.0 (1–5)	2.4 ± 0.8 (1–4)	0.593
	Left	Ant	1.4 ± 0.6 (1–3)	1.8 ± 0.5 (1–3)	0.011*	1.3 ± 0.5 (1–2)	1.9 ± 0.6 (1–3)	0.001**
		Post	2.1 ± 0.8 (1–4)	2.6 ± 0.9 (1–4)	0.064	2.4 ± 0.9 (1–5)	2.5 ± 1.0 (1–5)	0.059

ant anterior, *post* posterior

*p value ≤ .05

**p value ≤ .0017 (Bonferroni correction)

3, $N_{reader2,7T}$ = 2). For none of the exams, the artifact level was classified as *severe*.

Rootlet delineation

In general, anterior and posterior rootlets were well visualized by both 3 T and 7T MR exams (Figs. 1, 2a, 2b, and 3). Most of them were classified as *sharp* ($N_{reader1,3T}$ = 12, $N_{reader1,7T}$ = 12; $N_{reader2,3T}$ = 14, $N_{reader2,7T}$ = 11) or *moderate delineation* ($N_{reader1,3T}$ = 7, $N_{reader1,7T}$ = 7; $N_{reader2,3T}$ = 6, $N_{reader2,7T}$ = 7). Few were considered *poor delineation* ($N_{reader1,3T}$ = 2, $N_{reader1,7T}$ = 2; $N_{reader2,3T}$ = 1, $N_{reader2,7T}$ = 3). No difference was found between the field strengths regarding the subjective evaluation of the delineation of rootlets by both readers (*p* values of 0.5 and 0.2, respectively).

Number of rootlets

The results of both readers for the evaluation of rootlets are summarized in Table 2. The mean number of rootlets per root was higher at 7 T than at 3 T at every assessed level but this difference was not statistically significant (*p* range: 0.002–0.53). The mean number of posterior rootlets was larger ($mean_{reader1,3T}$ = 2.6, $mean_{reader1,7T}$ = 3.1) than that of the corresponding anterior rootlets ($mean_{reader1,3T}$ = 1.9, $mean_{reader1,7T}$ = 2.2).

Interobserver agreement

Considering the evaluation of artifacts and evaluation of delineation, the interobserver agreement was substantial to almost perfect with weighted κ values of 0.69 and 0.82 respectively. No difference was found between 3-T and 7-T image

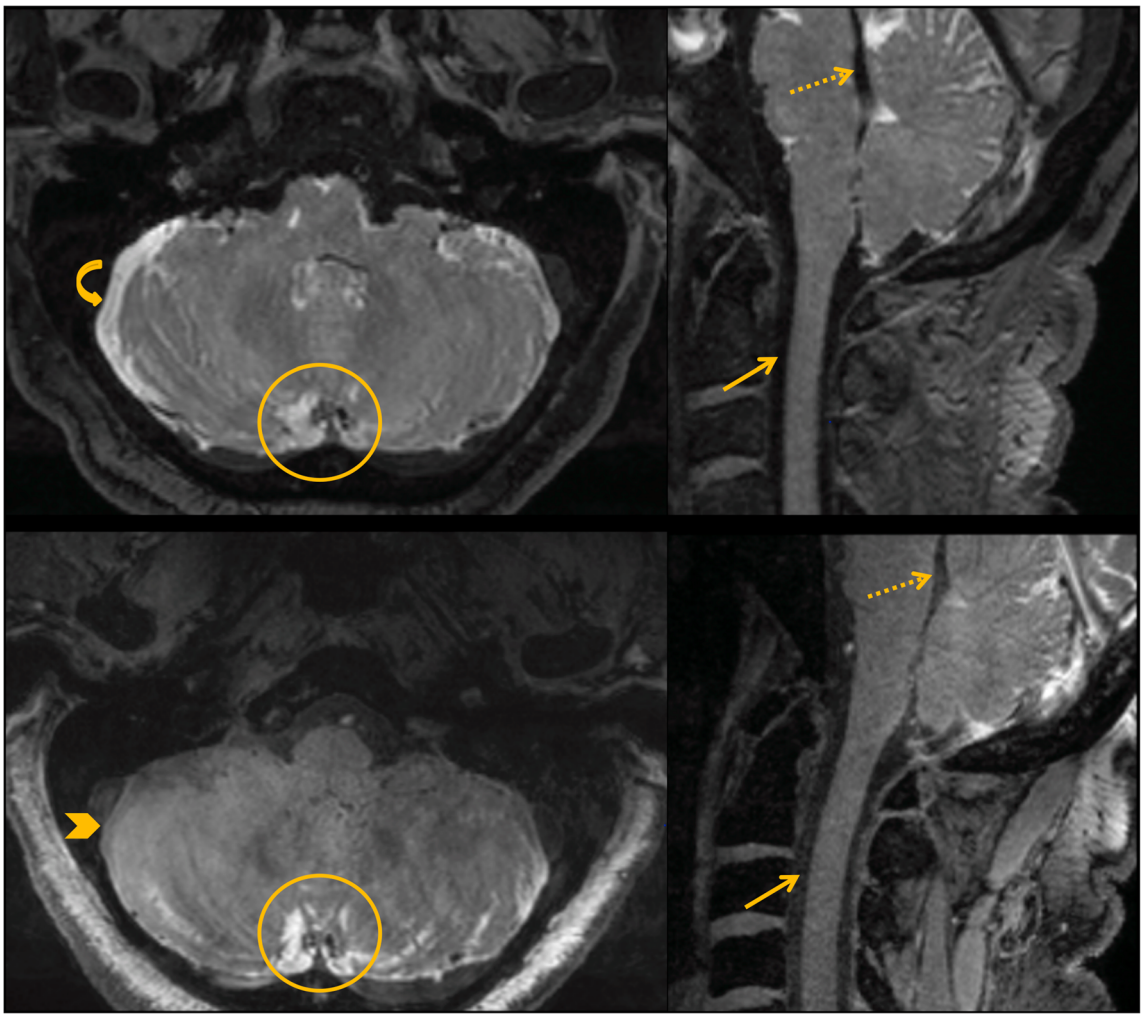

Fig. 4 Axially and sagittally reconstructed MPR images of a 59-year-old female patient. *Top*: 3T, *bottom*: 7T. The cerebrospinal fluid around the cord (orange arrows) and in the aqueduct (dotted arrows) is dark on both 3-T and 7-T images. In contrast, fluid in the vermian cistern appears bright (orange circle) at both field strengths, while pericerebellar fluid is depicted bright on 3-T images (curved arrow) and with intermediate signal intensity in the 7-T images (arrowhead)

evaluation. For the count of the number of rootlets, the intraclass correlation coefficient was 0.80.

Discussion

This study demonstrates the feasibility of a non-invasive visualization of parts of the intraspinal cervical rootlet in a cervical-spine patient cohort by means of dual echo steady state (DESS) MR-imaging at 3 T and at 7 T. In comparison with 3-T MRI, 7-T MRI allowed the identification of a higher number of rootlets but this difference was not statistically significant.

The DESS sequence has been proven to be of great value in optimizing the contrast between fluid and adjacent structures like cartilage [18]. Its 3D acquisition offers a high, isotropic spatial resolution in an acceptable scanning time, allowing multiplanar reformatting. Thus, 3D-DESS has become a valuable tool, e.g., for cartilage assessment [19–21]. We found only one study that evaluated neural structure by means of DESS imaging and demonstrated a good visualization of the intraparotid course of the facial nerve [22]. Our study was the first to assess cervical-nerve and intraspinal-rootlet visualization at high field. Potentially somewhat surprising, the excellent contrastation of the rootlets was made possible by the fact that the cerebrospinal fluid was mostly imaged dark by the DESS sequence. Typically, low-viscous, stationary fluids, e.g., intra-articular fluid, show a high signal intensity and a bright image on DESS images reflecting the T2-weighting contribution to the image-contrast weighting of the sequence. However, the signal intensity of the DESS sequence is also known to be strongly affected by motion. Thus, we hypothesize that the cerebrospinal fluid (CSF) signal was attenuated by flow-induced displacement in our acquisitions. As shown in Fig. 4, the cerebral fluid surrounding the cervical cord, as well as in the cerebral aqueduct, was dark, on 3-T as well as on 7-T images. On the contrary, in the vermian cistern, the fluid was bright at both fields and, in the pericerebellar fluid, had an intermediate signal on 7 T and high signal on 3 T. The different appearances of the cerebrospinal fluid could reflect different flow velocities in the corresponding anatomical structures.

The qualitative analysis of rootlets delineation did not show any statistically significant difference between 3- and 7-T images; however, it has to be kept in mind that our grading had only three levels (sharp, moderate, and poor) and can be subjective. A more detailed grading could potentially show differences.

The number of posterior rootlets depicted using MRI was lower in comparison to previous anatomical studies, where an average of 8 rootlets was described for the posterior root [1–3]. In part, this can be explained by our counting methodology. To be taken into account for our analysis, a rootlet had

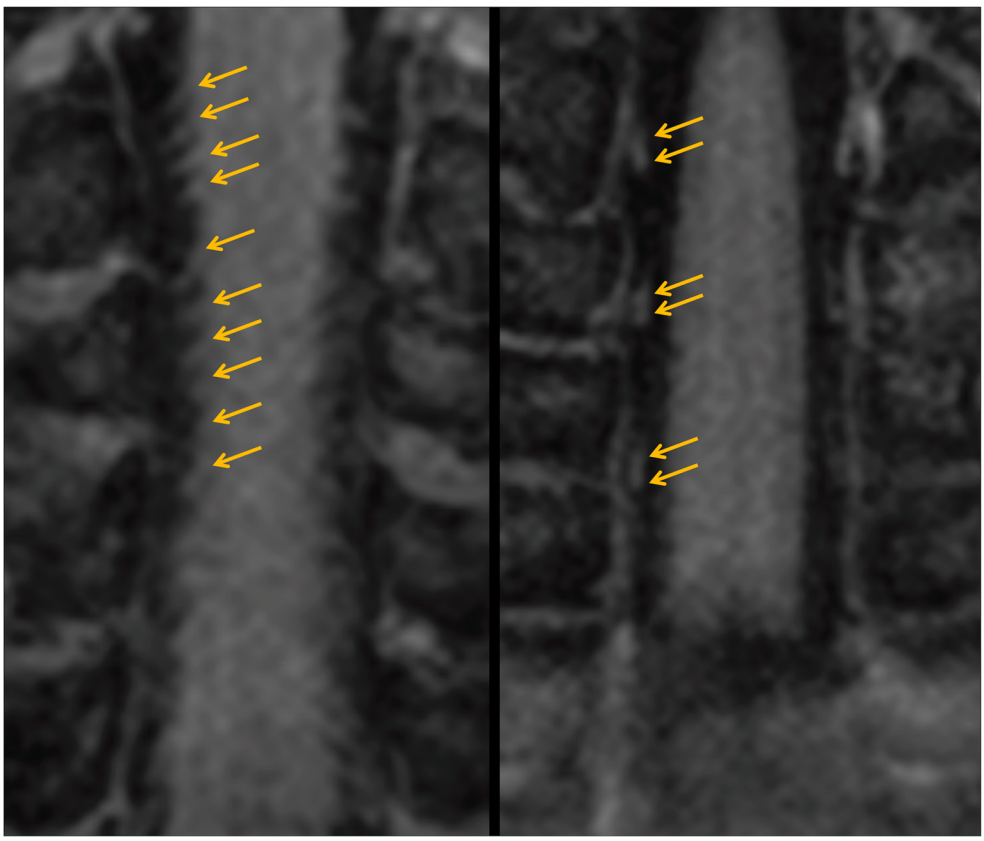

Fig. 5 Coronal 3-T images of a 59-year-old female patient. Directly at the level of posterior nerve-rootlet emergence (*left*) from the spinal cord, more rootlets (orange arrows) can be positively identified than in more lateral areas (*right*)

to be continuously visualized from its emergence from the cord to the fusion point with the corresponding anterior/posterior rootlet. However, many rootlets would combine (or fuse) before the anteroposterior root fusion. Thus, we would expect to identify a larger number of rootlets the closer we are to the cord. Indeed, as shown in Fig. 5, at the level of emergence, clearly more rootlets could be identified than more distally. However, we hypothesize that, in addition to rootlet fusion, the number of visualized intra-spinal rootlets may also decline with increasing distance from the cord due to motion of the rootlets, e.g., induced by CSF pulsation. This may be associated with a larger range of spatial displacement in more distant areas of the intraspinal rootlets from their points of emergence from the cord and the intervertebral foramen and may have contributed to the lower number of intra-spinal nerve rootlets identified in our non-invasive in vivo study, compared to anatomical post-mortem studies.

In the case of traumatic brachial plexus lesions, the distinction between pre- and postganglionic injuries is crucial for the treatment and prognosis [23, 24]. The direct visualization by MRI of the avulsed roots or rootlets is difficult and the presence of indirect surrogate findings as pseudomeningoceles, spinal cord signal changes, enhancement of nerve roots, or alteration of denervated muscle are all useful but inconsistent [8, 11, 25]. Thus, the use of the 3D-DESS sequence in suspicion of root avulsions could potentially be of a great value.

While interpreting the results of our study, it should be kept in mind that only a small patient cohort of 21 subjects was examined, which may not be representative of the population in everyday practice. Also, apparent differences observed for the exams at the two field strengths should cautiously be interpreted, considering that the respective imaging protocols were not systematically optimized and tailored for optimum comparability.

Nevertheless, this study successfully demonstrated the capability of 3D-DESS MR-imaging at high fields to visualize parts of the micro-anatomy of the intraspinal cervical nerve rootlets in a cervical-spine patient cohort. This could open possibilities for changing the way of assessing the pathology of the cervical nerve in the near future.

Funding The authors state that this work has not received any funding.

Compliance with ethical standards

Guarantor The scientific guarantor of this publication is Daniel Nanz.

Conflict of interest Balgrist University Hospital of Zurich as well as Balgrist Campus AG each has a research agreement with Siemens Healthcare AG.

Statistics and biometry One of the authors has significant statistical expertise.

No complex statistical methods were necessary for this paper.

Informed consent Written informed consent was obtained from all subjects (patients) in this study.

Ethical approval Institutional Review Board approval was obtained.

Methodology
- Prospective
- performed at one institution

References

1. Leijnse JN, D'Herde K (2016) Revisiting the segmental organization of the human spinal cord. J Anat 229(3):384–393
2. Alleyne CH, Cawley CM, Barrow DL, Bonner GD (1998) Microsurgical anatomy of the dorsal cervical nerve roots and the cervical dorsal root ganglion/ventral root complexes. Surg Neurol 50(3):213–218
3. Karatas A, Caglar S, Savas A, Elhan A, Erdogan A (2005) Microsurgical anatomy of the dorsal cervical rootlets and dorsal root entry zones. Acta Neurochir (Wien) 147(2):195–199 discussion 199
4. Carette S, Fehlings MG (2005) Clinical practice. Cervical radiculopathy. N Engl J Med 353(4):392–399
5. Caridi JM, Pumberger M, Hughes AP (2011) Cervical radiculopathy: a review. HSS J 7(3):265–272
6. Expert Panel on Neurological Imaging, Mc-Donald MA, Kirsch CFE, Amin BY et al (2019) ACR Appropriateness Criteria® cervical neck pain or cervical radiculopathy. J Am Coll Radiol 16(5S): S57–S76
7. Tharin BD, Kini JA, York GE, Ritter JL (2014) Brachial plexopathy: a review of traumatic and nontraumatic causes. AJR Am J Roentgenol 202(1):W67–W75
8. Yoshikawa T, Hayashi N, Yamamoto S et al (2006) Brachial plexus injury: clinical manifestations, conventional imaging findings, and the latest imaging techniques. Radiographics. 26(Suppl 1):S133–S143
9. Expert Panel on Neurologic Imaging, Bykowski J, Aulino JM, Berger KL et al (2017) ACR Appropriateness Criteria® Plexopathy. J Am Coll Radiol 14(5S):S225–S233
10. Expert Panel on Neurological Imaging and Musculoskeletal Imaging, Beckmann NM, West OC, Nunez D et al (2019) ACR Appropriateness Criteria® suspected spine trauma. J Am Coll Radiol 16(5S):S264–S285
11. Wade RG, Takwoingi Y, Wormald JCR et al (2019) MRI for detecting root avulsions in traumatic adult brachial plexus injuries: a systematic review and meta-analysis of diagnostic accuracy. Radiology. 293(1):125–133
12. Chhabra A, Thawait GK, Soldatos T et al (2013) High-resolution 3 T MR neurography of the brachial plexus and its branches, with emphasis on 3D imaging. AJNR Am J Neuroradiol 34(3):486–497
13. Yang J, Qin B, Fu G et al (2014) Modified pathological classification of brachial plexus root injury and its MR imaging characteristics. J Reconstr Microsurg 30(3):171–178
14. Lee JH, Cheng K-L, Choi YJ, Baek JH (2017) High-resolution imaging of neural anatomy and pathology of the neck. Korean J Radiol 18(1):180–193
15. Barry RL, Vannesjo SJ, By S, Gore JC, Smith SA (2018) Spinal cord MRI at 7T. Neuroimage. 168:437–451
16. Sigmund EE, Suero GA, Hu C et al (2012) High-resolution human cervical spinal cord imaging at 7 T. NMR Biomed 25(7):891–899

17. Yoon D, Biswal S, Rutt B, Lutz A, Hargreaves B (2018) Feasibility of 7T MRI for imaging fascicular structures of peripheral nerves. Muscle Nerve 57(3):494–498
18. Hardy PA, Recht MP, Piraino D, Thomasson D (1996) Optimization of a dual echo in the steady state (DESS) free-precession sequence for imaging cartilage. J Magn Reson Imaging 6(2):329–335
19. Peterfy CG, Schneider E, Nevitt M (2008) The osteoarthritis initiative: report on the design rationale for the magnetic resonance imaging protocol for the knee. Osteoarthritis Cartilage 16(12):1433–1441
20. Chaudhari AS, Black MS, Eijgenraam S et al (2018) 5-Minute knee MRI for simultaneous morphometry and T2 relaxometry of cartilage and meniscus and for semi-quantitative radiological assessment using double-echo in steady-state at 3T. J Magn Reson Imaging 47(5):1328–1341
21. Schleich C, Hesper T, Hosalkar HS et al (2017) 3D double-echo steady-state sequence assessment of hip joint cartilage and labrum at 3 Tesla: comparative analysis of magnetic resonance imaging and intraoperative data. Eur Radiol 27(10):4360–4371
22. Qin Y, Zhang J, Li P, Wang Y (2011) 3D double-echo steady-state with water excitation MR imaging of the intraparotid facial nerve at 1.5T: a pilot study. AJNR Am J Neuroradiol 32(7):1167–1172
23. Shin AY, Spinner RJ, Steinmann SP, Bishop AT (2005) Adult traumatic brachial plexus injuries. J Am Acad Orthop Surg 13(6):382
24. Terzis JK, Kostopoulos VK (2007) The surgical treatment of brachial plexus injuries in adults. Plast Reconstr Surg 119(4):73e–92e
25. Rankine JJ (2004) Adult traumatic brachial plexus injury. Clin Radiol 59(9):767–774